Model reduction in the back step fluid–thermal problem with variable geometry

E. Bache , J.M. Vega , A. Velazquez

Aerospace Propulsion and Fluid Mechanics Department, School of Aeronautics, Universidad Politecnica de Madrid, Plaza del Cardenal Cisneros 3, 28040 Madrid, Spain
Applied Mathematics Department, School of Aeronautics, Universidad Politecnica de Madrid, Plaza del Cardenal Cisneros 3, 28040 Madrid, Spain

ARTICLE INFO

Keywords:
Proper orthogonal decomposition
Reduced-order model
Variable geometry

ABSTRACT

A methodology is presented to undertake the development of reduced-order models (ROMs) in variable geometry fluid–thermal problems using the method of snapshots. First, some snapshots are calculated in computational domains that vary in both shape and number of grid points. These snapshots are projected onto a so-called *virtual grid* (defined in a *virtual geometry*) using a smooth transformation. Proper orthogonal decomposition (POD) modes are obtained from the associated *virtual snapshots* and projected back onto the original grids, where they are used to define expansions of the flow variables. The associated POD mode amplitudes are obtained minimizing a residual, which is calculated in terms of the reconstructed solution. POD modes are calculated using only a part of the computational domain, which will be called the *projection window*, and the residual is defined using only a limited number of points of the computational domain. This methodology is illustrated addressing the problem of heat transfer downstream of a backward facing step in the 2-D steady, laminar regime, with three free parameters, namely the Reynolds number, the wall temperature, and the step height.

1. Introduction

Nowadays, and across many different technical disciplines, there is much interest in the development of reduced-order models (ROMs). The reasons are scientific as well as technical because a reliable ROM of an engineering system may contribute both to understanding the non-linear behavior of the system and to shortening the time needed to move from the lab into the market. For example, a ROM could be used for optimization purposes, thereby allowing for the possibility to have a mature engineering design very quickly. In this context, a comprehensive review of ROM developments up to 2004 has been presented by Lucía et al. [1].

Many published ROM developments deal with fixed geometry problems, even though a sizable number of engineering systems and products are characterized by the fact that some geometry parameters are to be chosen as a part of the design process. Thus, it is worthwhile to explore techniques that allow for the possibility of considering a geometry parameter on the same footing as the flow parameters such as, e.g., the Reynolds number. Pioneering work in this area was carried out by Attonen et al. [2], who studied the effect of grid deformation (with a constant number of grid points) on the ROM behavior in two test problems, namely the potential flows around a translating cylinder and over an oscillating panel. To deal with grid deformation, these authors proposed what they called a multi-POD approach. The idea was to use several POD-based ROMs obtained for various sets of grid deformations and to blend them. Transition from one model to another was based on criteria associated with grid deformation. Silva and Bartels [3], on the other hand, presented a ROM for the aeroelastic analysis of wings, based on a Volterra-type formulation; the ROM of the unsteady aerodynamics system in state-space form was developed using modal input responses. Fluid–structure interaction has been also considered by Vierendeels et al. [4]. Their method focused on partitioned solvers, using ROMs of the individual fluid and structural problems to improve convergence of the fixed-point iterations of the complete formulation. It is to be noted that in this case, like in the others discussed previously, the computational grid undergoes deformations that preserve the number of mesh points.

A different type of real-time deformable system being analyzed by model reduction techniques has been reported by Niroomandi et al. [5], who obtained a ROM of the highly non-linear material deformation of the human cornea. Here, piece-wise polynomials were used to interpolate in the displacement field. On the other hand, small motions of a surface immersed in a flow field (membranes, typically) have been analyzed by the so-called implicit condensation method, where the effects of membrane displacements are condensed into the non-linear stiffness terms of the bending equations. However, this method does not allow for recovering membrane stresses. Recently, Hollkamp and Gordon [6] have proposed to use a membrane basis where membrane displacements are expanded

Nomenclature

A	Unknown expansion amplitude
BC	Boundary condition
$E_1 \ldots E_4$	Left hand sides of equations (1)–(4)
H	Dimensionless step height
k	Thermal conductivity
N	Direction normal to the wall
N	Size of the covariance matrix
p	Pressure
P_i	Expansion of p
Pr	Prandtl number
q'	Dimensional heat flux
R	Covariance matrix
Re	Reynolds number
ROM	Reduced-order Model
T	Temperature
T_i	Expansion of T
u	Horizontal velocity component
U_i	Expansion of u
v	Vertical velocity component
V_i	Expansion of v
x	Horizontal coordinate
y	Vertical coordinate

Greek Symbols

α	Expansion coefficient
Δ	Laplacian operator
η	Transformed vertical coordinate
γ	Eigenvalue of the covariance matrix
μ	Viscosity
Ω	Projection window

Subscripts

inlet	Inlet conditions
middle	Middle mesh node
R	Reattachment length
w	Wall
drop	Pressure drop

directly into the modal bending amplitudes. Finally, although not directly related to the work presented in this article, it is worthwhile to mention the developments of Mignolet and Soize [7], who presented a general method to deal with both parameter and geometric model uncertainty in dynamic problems involving linear structures and local non-linearities.

At this stage, it is also worth mentioning some recent developments in the generic field of model reduction. Rouizi et al. [8] have applied the modal identification method to, precisely, the back step flow problem in the laminar steady regime. Their identification procedure is formulated as an inverse problem of parameter estimation and the optimization algorithm is based on a gradient-type approach. Balima et al. [9] presented a detailed comparison in terms of both accuracy and required CPU time between the modal identification method and the POD-Galerkin approach, using a specific non-linear unsteady heat conduction test problem. Also, some new versions of the snapshot based balanced truncation method [10,11] allow for treating very high dimensional systems arising in optimal control of some time-dependent linear problems.

The main object of the present article is to describe a method to deal with model reduction in flow situations in which both geometry and flow parameters are allowed to change. The method is based on a methodology to develop ROMs in fixed geometry problems, already presented in [12] and further developed in [13] by two of the authors. In addition to shape variation, changes are allowed in the number of grid points required in the computational domain used to generate the snapshots. The method itself does not depend on the specific problem under consideration. However, for the sake of clarity we shall describe the method applying it to a specific test problem, with two ideas in mind:

- The application is only considered to illustrate the method. We do not intend to perform a complete study of the test problem, which includes various interesting bifurcations and instabilities.
- We shall focus on the advantages of the method concerning robustness and flexibility. The method can be further improved in various ways (see Section 5 below), but such improvements are beyond the scope of this paper.

The method can be summarized as follows. First, (i) Some snapshots are calculated using computational fluid dynamics (CFD) in computational grids that are defined by requirements of the CFD method. Then, (ii) The snapshots are smoothly transformed into a *virtual grid*, defined in a *virtual geometry*; a POD basis is calculated from the virtual snapshots. (iii) These POD modes are projected back onto the original (CFD) grids, and used to reconstruct the flow variables as an expansion of the modes. (iv) The corresponding POD mode amplitudes are obtained minimizing a residual, which is calculated using only a limited number of points of the CFD grid, located in a projection window.

Note that this method is conceptually simpler than other methods used so far to deal with derivation of ROMs in variable geometry problems. A natural question arises about whether POD modes obtained in the virtual geometry, from snapshots calculated in the various original geometries, will represent well (namely, with a few number of POD modes) the solution in the original geometries. We anticipate that the answer is yes. This is due to the very essence of POD, which describes well complex flow patterns using only a few modes provided that the snapshots show some (implicit) redundancies. With a fixed geometry, these redundancies are due to the fact that the state variables satisfy everywhere the governing partial differential equations. The geometry transformation just adds a smooth mapping (from the original grids to the virtual grid) to the governing equations. Thus, the method does not break (just transforms) the implicit redundancies of the problem.

In what follows, the test problem is described first, in Section 2. Then, the method is developed in Section 3 and results are presented and discussed in Section 4. Finally, some conclusions and guidelines for the method's application are given in Section 5.

2. Test problem description

We consider a well-known test problem, which has been used in a variety of theoretical, numerical, and experimental investigations, namely the laminar, non-isothermal, 2-D flow past a backwards facing step of variable step height (see Fig. 1). A comprehensive summary of experimental and numerical results of this problem can be found in the review article by Abu-Malaweh [14].

In the equations and boundary conditions below, all distances were rendered dimensionless using the hydraulic diameter of the inlet channel (twice the inlet height). The velocity, pressure, and temperature are non-dimensonalized with the mean inlet velocity,

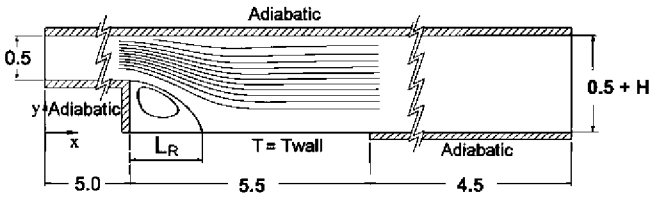

Fig. 1. Sketch of the test problem configuration. Flow moves from left to right.

the inlet dynamic pressure, and the inlet temperature, respectively. The length of the computational domain is 15 units. The step corner is located at $x = 5$. Walls are adiabatic except in a portion, 5.5 units long located downstream of the step, where the temperature is prescribed. The governing equations (continuity, horizontal and vertical momentum conservation, and energy conservation) are

$$\partial_x u + \partial_y v = 0 \tag{1}$$

$$u\partial_x u + v\partial_y u + \partial_x p - \frac{1}{\mathrm{Re}}\left[\mu\Delta u + 2\partial_x\mu\partial_x u + \partial_y\mu\left(\partial_y u + \partial_x v\right)\right] = 0 \tag{2}$$

$$u\partial_x v + v\partial_y v + \partial_y p - \frac{1}{\mathrm{Re}}\left[\mu\Delta v + 2\partial_y\mu\partial_y v + \partial_x\mu\left(\partial_x v + \partial_y u\right)\right] = 0 \tag{3}$$

$$u\partial_x T + v\partial_y T - \frac{1}{\mathrm{RePr}}\left[\kappa\Delta T + \partial_x\kappa\partial_x T + \partial_y\kappa\partial_y T\right] = 0 \tag{4}$$

where ∂_x and ∂_y stand for partial derivatives, $\Delta = \partial^2_{xx} + \partial^2_{yy}$ is the Laplacian operator, and μ and κ are the dimensionless (temperature dependent) viscosity and thermal conductivity, see eqs. (10) and (11) below. The inlet Reynolds and Prandtl numbers are defined as

$$\mathrm{Re} = 2\tilde{\rho}_{inlet}\tilde{h}_{inlet}\tilde{u}_{inlet}\Big/\tilde{\mu}\left(\tilde{T}_{inlet}\right), \mathrm{Pr} = \tilde{c}_p\tilde{\mu}\left(\tilde{T}_{inlet}\right)\Big/\tilde{\kappa}\left(\tilde{T}_{inlet}\right), \tag{5}$$

where the $\tilde{u}_{inlet}$ is the mean, dimensional inlet velocity and tildes denote hereafter dimensional quantities. The boundary conditions are as follows. At the inlet section, $x = 0$, the velocity profiles and pressure gradient are assumed to be Poiseuille-like and the temperature is set equal to the coolant temperature, namely

$$u(y-H) = -24\left[(y-H)^2 - \frac{(y-H)}{2}\right], \quad v(y) = 0,$$
$$\partial_x p = \frac{-48}{\mathrm{Re}}, \quad T = 1, \tag{6}$$

Strictly speaking, this boundary condition (which is based on the assumption of fully developed flow) only applies in the upstream far field. However, as shown in [15], it can also be considered a good approximation at the inlet section of the computational domain, which is located at a distance of 10 times the inlet channel height upstream of the step. At the outlet section, $x = 15$, the flow is also assumed to be fully developed and thus the velocity, pressure gradient, and temperature profiles do not longer depend on the x coordinate, namely

$$\partial_x u = \partial_x v = \partial^2_{xx} p = \partial_x T = 0. \tag{7}$$

At the walls, no slip is imposed and the non-adiabatic part of the lower wall is assumed to stay at a non-dimensional temperature $T = T_{wall}$, while the remaining part of the lower wall and the upper wall are thermally insulated. Namely,

$$u = v = 0, \quad T = T_{\mathrm{wall}}, \tag{8}$$

if $5 < x < 10.5$ and $y = 0$, and

$$u = v = 0, \quad \partial_n T = 0 \tag{9}$$

in the remaining parts of the walls. Here, n stands for the direction normal to the wall. Note that we are stating boundary conditions for the pressure at both the entrance and the exit of the domain, which in principle are not necessary. But the additional boundary conditions are compatible with the rest of the boundary conditions and convenient to improve precision in the analysis presented in the following section.

The working fluid is water, whose viscosity, $\tilde{\mu}$, and thermal conductivity, $\tilde{\kappa}$, are temperature dependent. Assuming that the temperatures at the entrance and at the non-isothermal part of the lower wall are 293 K and 351.6 K respectively, viscosity varies by a factor of 3. Here, some well-known correlations [15] for water are used that can be written in terms of the dimensionless temperature, T, as

$$\mu = \frac{\tilde{\mu}}{\tilde{\mu}_{293K}} = 1 - 5.646\cdot(T-1) + 12.259\cdot(T-1)^2, \tag{10}$$

$$\kappa = \frac{\tilde{\kappa}}{\tilde{\kappa}_{293K}} = 1 + 0.786\cdot(T-1) - 1.176\cdot(T-1)^2. \tag{11}$$

The CFD computations needed to generate the snapshots are carried out with the numerical simulation method described in [15], using a Cartesian grid and a pseudo-compressibility approach to solve the time-dependent versions of equations (1)–(4). The snapshots are in fact the steady state solutions to these equations. Three free parameters are present, namely the Reynolds number, the wall temperature downstream of the step, and the step height. The maximum dimensionless wall temperature is 1.2, which corresponds to an actual temperature equal 351.6 K (78.6 °C). This has been chosen bearing in mind the future prospect of performing an associated experimental study. The maximum Reynolds number (400) is selected to preserve the hypothesis that the flow is two dimensional [15–18]. The step height is allowed to change in a rather wide range (0.1–0.6), which involves large changes in both the geometry and flow topologies. An idea of the severity of this change is provided in Fig. 2, where the streamlines patterns are shown for three representative cases. In particular, the reattachment lengths are 0.13, 1.97, and 4.98 units, which yield a factor of 38 between extreme cases.

Furthermore, the flow topology shown in Fig. 2-**bottom** exhibits two recirculation regions instead of only one. As a result of such a variety of behavior, solving the problem also requires drastic changes in the computational mesh, both in the number of points (which are 6347, 12,485, and 16,577 in the three cases considered in Fig. 2) and in their distribution (which involves drastic changes of mesh size, see below).

Initially, *snapshots* are computed for the following 210 combinations of parameters:

- Reynolds number, Re = 100, 150, 200, 250, 300, 350, and 400 (7 values).

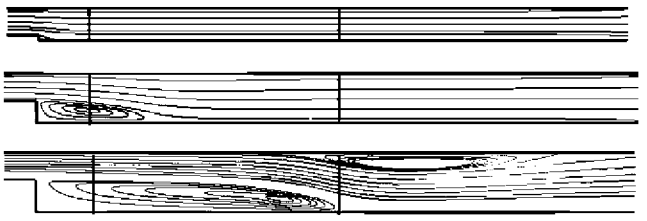

Fig. 2. Streamlines for the cases: Re = 100, Tw = 1.0, $H = 0.1$ (top), Re = 200,Tw = 1.1, $H = 0.4$ (middle), and Re = 400, Tw = 1.2, $H = 0.6$ (bottom). The projection window is indicated with thick solid lines in these three CFD domains.

Table 1
Definition of test points and CFD values of the figures of merit.

Test point	Problem parameters			Figures of merit		
	Re	Tw	*H*	L_R	P_{drop}	*Nu*
P01	225	1.075	0.35	1.783	1.094	3.202
P02	275	1.125	0.45	2.917	0.727	5.347
P11	125	1.025	0.15	0.317	3.318	1.088
P12	125	1.175	0.15	0.383	3.026	8.702
P13	125	1.025	0.55	1.983	1.963	0.734
P14	125	1.175	0.55	2.167	1.910	5.980
P15	375	1.025	0.15	0.683	0.921	1.507
P16	375	1.175	015	0.817	0.836	12.21
P17	375	1.025	0.55	4.350	0.417	0.905
P18	375	1.175	0.55	4.400	0.420	7.748

- Wall temperature, $T_{wall} = 1.0, 1.05, 1.10, 1.15$, and 1.20 (5 values).
- Step height, $H = 0.1$, 0.2, 0.3. 0.4, 0.5, and 0.6 (6 values).

Later on (see below), one additional series of snapshots will be computed in the case $H = 0.15$ to improve results, which will increase the total number of snapshots to 245.

To assess the ROM accuracy, a series of 10 *test points* has been defined inside the parametric space, see Table 1. The first two points (P01 to P02) are well inside the parametric space and thus represent a typical application of the method. The remaining eight points (P11 to P18) are located near the corners of the parametric space and have been chosen to test the applicability limits of the method.

Three *figures of merit* have been chosen to compare the ROM and CFD results, namely the reattachment length, L_R, of the recirculation region located directly downstream of the step (to somehow account for the flow topology), the pressure drop, P_{drop}, between entrance and exit (a measure of the required pumping power), and the heat flux (a measure of the thermal efficiency) across the heated portion of the lower wall behind the step (see Fig. 1). The latter is accounted for using the Nusselt number, defined as

$$Nu = \frac{\tilde{Q}'}{2\left(\tilde{T}_{\max,\text{wall}} - \tilde{T}_{inlet}\right)\,\kappa(T_{\text{wall}})\,\tilde{h}_{inlet}} \equiv \int_5^{10.5} \partial_y T(x,0)\mathrm{d}x \qquad (12)$$

where $\tilde{Q}'$ is the dimensional heat flux across the non-adiabatic part of the lower wall. The actual CFD values of these figures of merit at the test points are given in Table 1

3. Method description

The method proposed to develop a ROM with variable geometry is now described.

Table 2
Relative errors resulting from both HOSVD + interpolation and ROM calculations on the reattachment length, the pressure drop, and the heat flux, using 210 snapshots and 15 modes. POD modes are calculated in the projection window (19) and the residual is calculated from 50 equispaced points in the projection window (27).

Test point	HOSVD + interpolation Error in %			ROM Error in %		
	L_R	P_{drop}	*Nu*	L_R	P_{drop}	*Nu*
P01	0.0	0.5	0.4	1.9	0.4	0.1
P02	1.1	0.2	2.1	1.1	0.1	2.2
P11	10.5	3.6	0.0	10.5	2.5	4.0
P12	8.7	3.4	0.5	13.0	2.4	0.4
P13	0.8	2.8	0.5	0.0	1.0	1.0
P14	0.8	2.8	0.1	0.8	7.1	0.2
P15	14.6	1.8	1.3	17.1	1.4	1.3
P16	14.3	1.7	1.2	14.3	0.9	1.0
P17	1.5	0.5	6.7	1.9	0.5	8.4
P18	0.4	0.5	2.2	0.4	0.3	2.0

3.1. Virtual geometry and virtual mesh

The mesh used in the CFD calculations is separated into 5 different zones, as plotted in Fig. 3, top. Mesh spacing is different in the five zones, as required to appropriately describe those zones of greater flow complexity. Furthermore, some abrupt changes in mesh size are present at the zone boundaries, which could cause local errors in the calculations and some difficulties in establishing relationships between the different geometries created by the varying step height. A close-up view of the near-corner CFD grid distribution is shown in Fig. 3, bottom.

These geometries and mesh topologies cannot be used in a standard POD, which requires a fixed geometry (with fixed mesh points). Thus, a *virtual geometry* is first defined as the case with a step size $H = 0.3$. In this, a *virtual mesh* is defined as the Cartesian equispaced mesh with five zones that are the counterparts of the zones in the CFD meshes. In both cases the X–Y spacing between mesh points is as follows: zone 1: 0.1×0.05, zone 2: 0.01667×0.05, zone 3: 0.01667×0.01667, zone 4: 0.45×0.05, zone 5: 0.45×0.01667.

Now, transformation between the virtual geometry and the actual geometries for each value of the step height H is done mapping the vertical coordinate, using the logarithmic function

$$\eta = A\ln(By + 1), \qquad (13)$$

where A and B are determined requiring that $\eta(H) = 0.3$ and $\eta(H + 0.5) = 0.8$, which preserves both the step and channel heights. These yield two equations,

$$A\ln(B(H + 0.5) + 1) = 0.8, \quad A\ln(BH + 1) = 0.3, \qquad (14)$$

which uniquely determine A and B in terms of H and are solved using a standard iterative solver such as that in Maple. Note that while y varies between 0 and $0.5 + H$, the virtual vertical coordinate η varies between 0 and $0.5 + 0.3 = 0.8$. In fact, other functions, $\eta = f(y)$, can be used with the only requirements that they be smooth and that $f(0) = 0$, $f(H) = 0.3$, and $f(H + 0.5) = 0.8$. The logarithmic function (13) has been selected because it exhibits a nearly linear growth in the upper part of the domain.

Now, the state variables, u, v, p, and T must be transformed back and forth between the original and virtual meshes, which is done using the transformation (13) and cubic spline interpolation in both the original and virtual meshes.

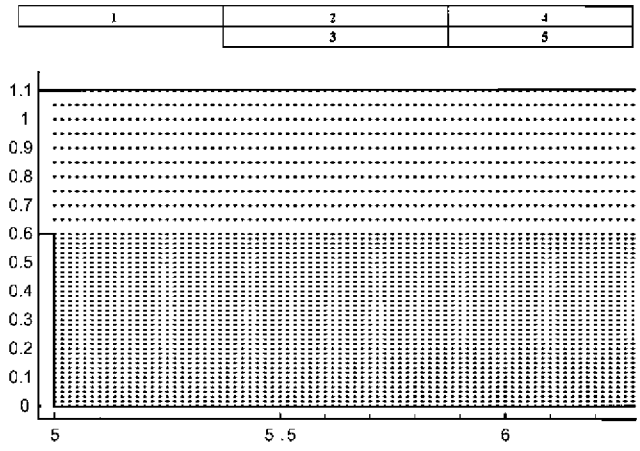

Fig. 3. Top: overview of a typical CFD domain with the different zones. Bottom: grid points distribution in the vicinity of the step for the case $H = 0.5$.

3.2. Snapshots, POD modes, and POD plus interpolation

The snapshots are computed with the CFD method presented in [19] and must be representative of the parameter range we intend to cover. Each snapshot gives the steady state of the system for a specific set of values of the parameters; the snapshot is defined by the velocity components, pressure, and temperature, namely

$$(u_k, v_k, p_k, T_k) \quad \text{for } k = 1, \ldots, N. \tag{15}$$

These snapshots are first projected into the virtual geometry using (13) and then used to obtain the POD modes, which are calculated independently for each variable (a difference from the standard POD + Galerkin approach) using standard formulae. For instance, POD modes for the horizontal velocity are given by

$$U_j = \sum_{k=1}^{N} \alpha_j^k u_k, \tag{16}$$

where the coefficients α_j^k are such that $(\alpha_1^1, \ldots, \alpha_1^N), \ldots, (\alpha_N^1, \ldots, \alpha_N^N)$ are the eigenvectors of the positive definite, symmetric $N \times N$-matrix R, known as the *covariance matrix*, defined as

$$R_{ij} = \langle u_i, u_j \rangle \tag{17}$$

in terms of the usual L_2-inner product

$$\langle u_i, u_j \rangle = \int_{\Omega} u_i(x, \eta) u_j(x, \eta) \mathrm{d}x\mathrm{d}\eta, \tag{18}$$

where Ω is the following *projection window* in the virtual geometry

$$\Omega : 6 < x < 10, \quad 0 < y < 0.8, \tag{19}$$

which is the counterpart of the projection window in the CFD geometries that will be used below to define the residual, see equation (27) below.

The covariance matrix is sometimes [20] computed as $R_{ij} = \langle u_i - \overline{u}, u_j - \overline{u} \rangle$, where $\overline{u}$ is the average of u in the snapshots set. This is convenient, in particular, when $u_i - \overline{u}$ is somewhat small compared to $\overline{u}$. But such improvement is not essential in the analysis below, and will not be pursued.

The projection window (19) has been chosen such that it (a) covers most of the recirculation bubble attached to the step and (b) avoids the corner region near the upper part of the step, where CFD calculations show the largest localized errors due to a singularity in the velocity gradient. Note that we are not taking the whole fluid domain to calculate POD modes, as is usually done in standard POD + Galerkin approaches; this simplification has been explained and checked in reference [13].

Now, if the expansion (16) is truncated to $n \leq N$ terms, then the relative error in terms of the L_2-norm associated with the inner product (18) is bounded by

$$|error| \leq \sqrt{\sum_{i=n+1}^{N} \gamma_i \Big/ \sum_{i=1}^{N} \gamma_i} \tag{20}$$

where $\gamma_1 \geq \ldots \geq \gamma_N \geq 0$ are the eigenvalues of the covariance matrix (17), namely the squares of the *singular values*. This gives an a priori estimate of the number of POD modes that must be retained to obtain a fixed error.

After truncation and projection back into the CFD geometry, the POD modes are used to calculate the flow variables as

$$u(x, y) = \sum_{i=1}^{n_1} A_i^1 U_i(x, y), \quad v(x, y) = \sum_{i=1}^{n_2} A_i^2 V_i(x, y) \tag{21}$$

$$p(x, y) = \sum_{i=1}^{n_3} A_i^3 P_i(x, y), \quad T(x, y) = \sum_{i=1}^{n_4} A_i^4 T_i(x, y) \tag{22}$$

where the *POD mode amplitudes* $A_i^1, \ldots, A_i^4$ are unknowns to be determined below. Although the number of modes in each variable needs not be the same (see the comment on this subject below in Section 5), for simplicity we assume hereafter that

$$n_1 = \ldots = n_4 = n. \tag{23}$$

As an initial guess for the optimization process below, we shall use a first approximation of the amplitudes for arbitrary parameter values using *High Order Singular Value Decomposition (HOSVD) + interpolation* [21] (see also [22] for a former Singular Value Decomposition + interpolation method), which requires to take into account the parameter values for which the $N = N_1 \times N_2 \times N_3$ snapshots (15) have been calculated, namely

$$\mathrm{Re}_1, \ldots, \mathrm{Re}_{N_1}, \quad T_{\mathrm{wall},1}, \ldots, T_{\mathrm{wall},N_2}, \quad H_1, \ldots, H_{N_3}. \tag{24}$$

The amplitudes of the modes in terms of these parameters, namely

$$A_i^j = A_i^j(\mathrm{Re}, T_{\mathrm{wall}}, H), \tag{25}$$

are calculated in two steps: (a) at the parameter values associated with the snapshots (24), the POD mode amplitudes $A_i^j = A_i^j(\mathrm{Re}, T_{wall}, H)$ are obtained by just projecting the snapshots (15) into the POD basis, which requires projecting back and forth into the virtual mesh; and (b) at the remaining (intermediate) values of the parameters, each mode amplitude is calculated using HOSVD to obtain joint modes associated with dependence on the three parameters and cubic spline interpolation in each of these joint modes; we note that interpolation is done in one variable in each case, which is much more efficient than standard three dimensional interpolation; see [21] for more details.

3.3. The overall residual

As anticipated above, the next step consists in calculating the POD mode amplitudes (i.e. the coefficients in the expansions (21)–(22)) by minimizing the following residual (see [13])

$$\mathrm{Residual} = \sum_{j=1}^{4} \frac{1}{N_E} \sum_{k=1}^{N_E} |E_j(x_k, y_k)| + \sum_{j=1}^{4} \frac{1}{N_{BC}} \sum_{k=1}^{N_{BC}} |BC_j(x_k, y_k)|, \tag{26}$$

where (x_k, y_k) are all points in the following projection window

$$6 < x < 10; 0 < y < 0.5 + H, \tag{27}$$

which is the counterpart of the projection window in the virtual geometry that was used above to calculate POD modes (cf equation (19) and see Fig. 2). $E_1, \ldots, E_4$ are the left hand sides of eqs. (1)–(4) and

$$BC_1 = u(0, y_{middle}) - \left\{ -24(y_{middle} - H)\left[(y_{middle} - H) - \frac{1}{2}\right] \right\},$$

$$BC_2 = \frac{\partial p}{\partial x} - \left(-\frac{48}{\mathrm{Re}}\right) \approx \frac{p(\Delta x_{entrance}, y_{middle}) - p(0, y_{middle})}{\Delta x_{entrance} - 0} - \left(-\frac{48}{\mathrm{Re}}\right),$$

$$BC_3 = T(0, y_{middle}) - T_{entrance},$$

$$BC_4 = T\left(x_{heating}, y_{middle}\right) - T_{\mathrm{wall}},$$

account for the non-homogenous boundary conditions in (7)–(9). In particular, $p(\Delta x_{entrance}, y_{middle})$ is the pressure at the mesh node directly downstream of $p(0, y_{middle})$, T_{wall} is the imposed wall temperature, and $T(x_{heating}, y_{middle})$ is the temperature at the middle mesh node in the heated part of the lower wall. Note that only one point of the boundary is used to impose each boundary condition. This is because the boundary conditions only vary by a constant factor as the parameters are varied.

Now even though using a projection window instead of the whole fluid domain bears a saving in computational effort, the first term in (26) still involves all mesh points in the projection window and can lead to fairly expensive calculations if N_E is large. In order to avoid calculating the whole residual in each step of the iterative optimization process, we could have proceeded as usually done in Galerkin approaches [12], namely using a preprocessing that allows for replacing (26) by a polynomial expression in the unknown POD-amplitudes, whose coefficients can be calculated from the outset. This requires that we redefine (26) using a polynomial form of the residual, and also requires that we calculate a large number of coefficients of the polynomial, which may involve quite expensive calculations. Here, as in [13] we proceed in a less standard way, noting that the essence of the POD method is that all snapshots are well approximated by a small number of modes, which suggests that the residual could be calculated using only information from a also small number of mesh points, somewhat larger than the expected number of POD modes. This observation in [13] was new in the context of reduced-order modeling and can be justified in rough terms noting that if all solutions were exactly contained in the POD manifold and calculations were exact, then N_E could be taken (generically) equal to the dimension of the manifold, in order to have as many equations as the number of unknowns. Since calculations are not exact, N_E must be larger than the number of modes, but not necessarily equal to the number of mesh mesh points, which depends on the CFD method, not in the POD approximation itself. A more detailed description of the method can be found in [13], where the idea was checked in a thermal problem similar to the one considered here, obtaining that results are fairly independent of both the projection window and the number of selected mesh points, with only weak limitations. In the sequel, we only consider 50 equispaced points in the projection window to calculate the residual (26).

Now, the residual defined above can be minimized using various methods. Genetic Algorithms exhibit the advantage of being robust, which is convenient in the present work. It is clear that gradient-type methods are faster than genetic algorithms and thus would be more appropriate for practical engineering design applications in an industrial context. However, since the focus of this work is on the development of a ROM methodology with variable geometry, a robust (if not particularly efficient) optimization approach has been selected. Note that gradient-like operators cannot be applied to minimize the residual (26), which is not differentiable because of the absolute values that appear in the right hand side. Nevertheless, as further explained in [13], results would only slightly worsen if the residual (26) were replaced by, e.g.,

$$\text{Residual} = \sqrt{\sum_{j=1}^{4} \frac{1}{N_E} \sum_{k=1}^{N_E} E_j(x_k, y_k)^2} + \sqrt{\sum_{j=1}^{4} \frac{1}{N_{BC}} \sum_{k=1}^{N_{BC}} BC_j(x_k, y_k)^2},$$

which is differentiable and thus amenable to gradient-like methods. The parameters of the genetic algorithm used to compute the amplitudes in the modal expansions were: 10 bits per individual, 10,000 individuals in each population, 100 elite individuals that go over to the next generation, a crossover probability of 0.8, and a mutation probability such that 1% of individuals mutate one random bit. The CPU time needed to reach the solution with 15 modes (Tables 3 and 5) in a 3.20 GHz desktop computer was 3–7 min depending on the test case. It should be noted however that this time can be reduced if the number of generations is lowered; the number of generations used was chosen to overshoot the necessary amount.

Table 3
Same as Table 2, but using 245 snapshots and either 15 modes.

Test point	HOSVD + interpolation Error in %			ROM Error in %		
	L_R	P_{drop}	Nu	L_R	P_{drop}	Nu
P01	0.9	0.4	1.4	0.0	0.1	2.0
P02	1.1	0.2	2.4	1.1	0.2	2.5
P11	5.2	2.6	0.7	5.2	1.7	0.3
P12	4.4	2.5	0.1	8.7	1.2	0.2
P13	0.8	2.8	0.2	1.7	0.9	0.5
P14	0.8	2.8	0.1	0.8	0.6	0.3
P15	0.0	0.3	1.3	0.0	0.1	1.3
P16	2.0	0.4	0.8	2.0	4.0	5.4
P17	1.5	0.5	6.9	1.9	1.2	7.5
P18	0.4	0.5	2.4	0.4	0.2	2.1

4. Results

To begin with, the ROM developed above is applied using the 210 snapshots indicated in section 2 and retaining the 15 most energetic POD modes, calculated using the projection window (19); the residual is calculated using only 50 equispaced points in the projection window (27). Relative errors (in %) on the three figures of merit (namely, the reattachment length, the pressure drop, and the heat flux) at the test points are given in Table 2 as calculated using both HOSVD + interpolation (as described above) and the ROM; see Table 1 for the definition of the test points and the CFD-calculated values of the figures of merit. Note that both HOSVD + interpolation and ROM errors are always smaller than 4%, except for the reattachment length at test points P11, P12, P15, and P16 and the heat flux at test point P17. The reason for this lower accuracy seems to be due to the fact that POD approximations tend to deteriorate when either:

a) The step height is small (test points P11, P12, P15, and P16, see Table 1) because flow structures have a much smaller size than for larger values of H.
b) Or the wall temperature is lowest (test point P17), because heat transfer in this case is associated with small values of the heat flux near the walls.

Table 4
Same as Table 2, but using 245 snapshots and 30 modes.

Test point	HOSVD + interpolation Error in %			ROM Error in %		
	L_R	P_{drop}	Nu	L_R	P_{drop}	Nu
P01	0.9	0.4	0.2	0.9	0.2	0.1
P02	1.7	0.2	0.6	1.7	0.0	0.6
P11	0.0	2.5	0.5	0.0	1.5	0.5
P12	0.0	2.5	0.3	0.0	1.3	0.3
P13	0.8	2.8	1.0	0.8	1.4	1.0
P14	0.8	2.8	0.2	0.8	1.1	0.4
P15	0.0	0.2	0.7	0.0	0.2	0.3
P16	0.0	0.1	0.0	0.0	0.1	0.0
P17	0.0	0.5	3.0	0.0	0.4	2.2
P18	0.0	0.5	1.0	0.0	0.4	1.0

Table 5
Relative errors % on the figures of merit calculated with the ROM described in Table 3, but (left) using 70 + 30 points in the projection window (27), and (right) using two projection sub-windows, see (28) and (29).

	One window, 70 + 30 points			Two windows, 50 + 15 points		
Test point	L_R	P_{drop}	Nu	L_R	P_{drop}	Nu
P01	0.9	0.2	0.9	0.9	0.2	0.6
P02	1.7	0.1	2.3	1.7	0.1	2.4
P11	5.2	1.9	0.2	5.2	1.7	0.5
P12	0.0	1.3	1.5	0.0	1.3	0.7
P13	0.8	0.9	0.1	1.7	0.9	0.0
P14	0.8	0.6	0.3	0.8	0.6	0.3
P15	0.0	0.1	1.2	2.4	0.2	1.1
P16	2.0	1.0	2.7	0.0	0.3	0.8
P17	1.1	0.5	7.6	1.1	0.5	7.6
P18	0.4	0.1	2.2	0.4	1.6	2.2

In both cases, the actual numerical resolution in POD might be not sufficient. In order to deal with this difficulty, two improvements have been made in the method:

1. Increasing the number of snapshots with 35 additional ones at a step height $H = 0.15$. Results are given in Table 3 and show that results improve everywhere. Also, errors are now smaller than 2.4% (including the approximation of L_R at P15 and P16), except for the reattachment length at P11 and P12 and the heat flux at P17, which are exact only within 8.7%. In any event, deviations of this order are admissible from the point of view of, for example, micro–electro–mechanical systems (MEMS) design engineering applications since, in this context, experimental work has uncertainties of the order of ±10%.
2. Using the same 245 snapshots as in case (a), but retaining twice the number of modes (a total of 30, instead of 15). The results obtained are presented in Table 4, and show that now accuracy is quite good for the three figures of merit in the ten test points. Also, results obtained using the ROM (within 1.5% accuracy) are consistently better than those obtained using HOSVD + interpolation (2.8% errors). It is to be noted, however, that this improvement came at the expense of a larger computational time. While each run of the ROM in Table 3 is performed in only 3–7 CPU minutes, each run in Table 4 requires 10–30 min.

Now, the question is whether a similar agreement is found when flow variables are compared at the local level. Fig. 4 shows the streamline patterns in the step vicinity for test cases P01 and P17. Note that the agreement is quite good. The associated isobars and isotherms are given in Figs. 5 and 6, respectively. Agreement is again quite good, except of course at those regions where either pressure or temperature is almost constant, as was to be expected.

POD modes and the residual were calculated using data from the projection windows (19) and (27), which excluded that zone where the flow exhibits a second recirculation bubble at some test points. It is also noteworthy that only five of the snapshots exhibited the second recirculation bubble, and that the CFD grid were fairly sparse in that zone were the second bubble appears, see Fig. 3. In spite of these, the second recirculation bubble is reasonably well approximated, as shown in Fig. 7, where it is seen that discrepancies are mainly associated with a shift of the bubble position. Still, the main recirculation bubble is always well approximated even though the projection window excluded also the main recirculation bubble in some cases (Fig. 2-up) and a large part of this bubble in some other cases (Fig. 2-middle). All these illustrate both (a) the power of POD when this method is properly used and (b) the fact that the ROM is quite robust in the sense that selection of the projection window is not critical.

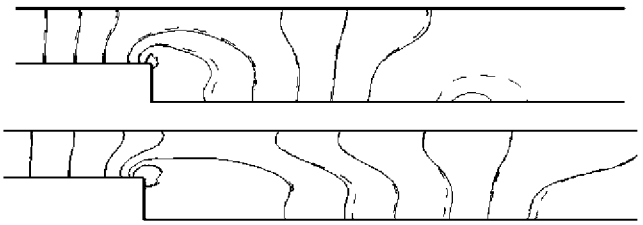

Fig. 5. Comparison between CFD (solid) and ROM (dashed) isobars at test points P01 (top) and P17 (bottom).

Now, a question arises on whether the results above can be improved with a better selection of both the projection window and the points where the residual are calculated. Concerning the latter, note that choosing 50 equispaced points in the projection window (27), as we did in Tables 2–4 to calculate the residual means that, for instance, that zone affected by the first recirculation bubble ($0 < y < H$) contains 18 points when $H = 0.1$ and 40 points when $H = 0.6$. This suggests two improvements:

- A first improvement results from maintaining the projection windows (19) and (27), but increasing the number of points in the residual calculation to 100, and ensuring that 70 of them are in that part of the projection window affected by the first recirculation bubble ($0 < y < H$). Results are shown in Table 5-left. Comparison with Table 4 shows that a significant improvement results from the increase in the number of points and the better selection of the 100 points. Note that errors are within 2.3% except for the reattachment length at point P11 and the heat flux at point P17; but note that the CFD values of L_R and heat flux at these points are quite small, which explains the larger relative errors.
- The projection window can be split into two sub-windows in such a way that they roughly cover those regions affected by the recirculation bubbles. Namely,

$$6 < x < 10;\ 0 < \eta < 0.3, \quad 9 < x < 13;\ 0.3 < \eta < 0.8 \tag{28}$$

$$6 < x < 10;\ 0 < y < H, \quad 9 < x < 13;\ H < y < 0.5 + H \tag{29}$$

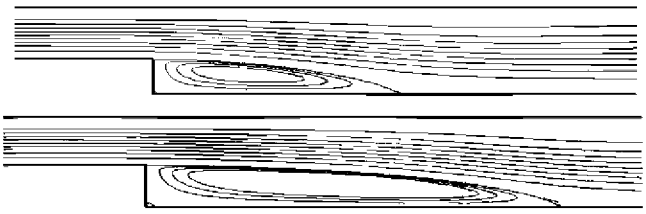

Fig. 4. Comparison between CFD (solid) and ROM (dashed) streamlines at test points P01 (top) and P17 (bottom).

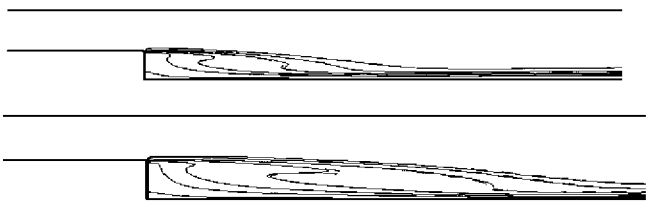

Fig. 6. Comparison between CFD (solid) and ROM (dashed) isotherms at test points P01 (top) and P17 (bottom).

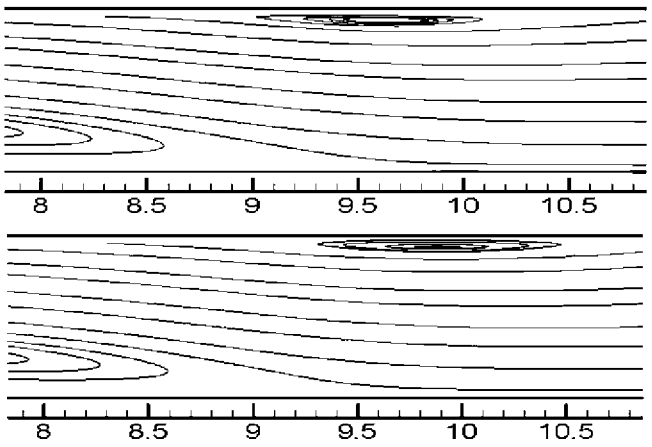

Fig. 7. Comparison between CFD (top) and ROM (bottom) streamlines in the region of the second recirculation bubble at test point P17.

in the virtual and CFD geometries, respectively. Also, the residual is calculated taking 50 and 15 points in the first $(6 < x < 10)$ and second $(9 < x < 13)$ sub-windows, respectively. Results are shown in Table 5-right and are quite similar to those resulting from the first improvement above, which shows that the whole process is quite robust.

5. Conclusions

A method has been presented to generate ROMs in fluid–thermal problems with variable geometry. In particular, the required CFD-calculated snapshots are obtained in computational domains with variable shape and number of grid points. Then, these snapshots are projected onto a virtual grid using a continuous smooth transformation. In this fashion, the resulting virtual snapshots are used to generate POD modes that, in turn, are projected back onto the set of initial computational domains. These POD modes are used as the basis for the expansion of the flow variables. The unknown coefficients of the expansion are obtained by minimizing a residual defined from the Navier–Stokes equations and boundary conditions. The residual is calculated using a few points in a projection window in the computational mesh, which can be selected subject to only weak limitations and contribute to CPU time saving. The projection window is calculated such that it includes at least a part of that portion of the fluid domain that exhibits a more defined structure (recirculation bubbles); avoiding those regions with CFD localized errors (corner regions) is also advisable.

The method has been illustrated by addressing the problem of non-isothermal laminar flow past a back step of variable height. We have considered, as a working fluid, water with temperature dependent viscosity and thermal conductivity.

The results obtained show that the method is flexible, robust, and accurate enough to be used for practical engineering applications. In particular, three parameters are considered in the test problem, namely the Reynolds number, the wall temperature, and the step height, which could be considered as representative of a variety of industrial problems in which flow topology, thermal, and geometry properties need to be analyzed simultaneously. Some remarks about the results are now in order:

1) When considering test points located well inside the 3-D parametric space (test points P1 and P2), the ROM global results (main recirculation region reattachment length, pressure drop, and heat flux) are within 2% of the CFD solution even with the simplest ROM configuration (210 snapshots, 15 POD modes, and residual calculated using 50 equispaced points in the simplest projection window). The spatial distribution of the computed variables is also close enough to the CFD solution to be used for detailed analysis purposes. The CPU time needed to generate each of these ROM results is of the order of 3 min, which is much smaller that the time needed to generate a CFD solution (of the order of 8–10 h).
2) The accuracy of the method degrades, as it could be expected when the selected test points are close to the boundary of the 3-D parametric space. In this case, discrepancies with the CFD solutions using the simplest ROM configuration (Table 2) are of the order of 3% except at some points where they can be as large as 17%. The time needed to generate the ROM model goes up to about 7 min. Adding some snapshots in the region of lower step height (Table 3) reduces the largest errors to 8.7%, which it is already acceptable for engineering purposes and still requires a CPU time of 7 min, which is quite competitive when compared to the time needed to generate a full CFD solution.
3) Accuracy can be increased either retaining more POD modes (30 instead of 15, Table 4), which gives excellent accuracy but requires a CPU time of 10–30 min (still competitive compared to CFD) or selecting better both the projection window and the points where the residual is calculated (Table 5). This gives both an excellent precision (errors within 3% except at those points where the approximated quantities are really small, where it is still reasonable, of the order of 7%) and a fairly small CPU time (3–7 min). Concerning the latter improvement, it is convenient that the projection window includes at least a part of the structured flow regions (e.g., second recirculation bubble), and that the selected points to calculate the residual are located in a balanced way, namely that there is a sufficient amount of them in the most structured regions. Nevertheless, the method is robust enough in connection with all these guidelines since, for instance reasonable results (even on the second recirculation bubble) are obtained selecting a projection window that does not contain the second recirculation bubble (or even does not contain the first recirculation bubble either, see Fig. 2), and calculating the residual using equispaced points in the first projection window, which puts only a few points in the first recirculation bubble.
4) For simplicity, we have retained the same number of POD modes in each flow variable, but this can of course be improved selecting an appropriate number of modes for each flow variable. This could be done in an efficient way using the a priori error estimate (20), which is based on the singular values of each POD.
5) Adding 15 additional snapshots in that region of the parameter space where the ROM results exhibited largest errors highly improves the efficiency at a reasonable computational cost. This opens the possibility of designing a method to select the snapshots in such a way that only a few of them are enough, if properly selected. Its number should be just somewhat larger than the number of POD modes (say, twice the number of modes). The method would provide a dramatic reduction in computational time, since this is essentially associated with the CFD calculations of the snapshots. The remaining calculations in the method are quite inexpensive after the improvements introduced above. Such method is well outside the scope of this paper, and the object of current research.
6) Gradient-like methods could be used to dramatically decrease computational time, which as explained above would require a redefinition of the residual and an efficient calculation of the gradient. Some care should also be taken with non-uniqueness of local minima of the residual, which is again under research.

Acknowledgements

This research was supported by the Spanish Ministry of Education and Science (MEC) under Projects DPI2009-07591 and TRA2007-65699. The authors gratefully acknowledge this support. The authors are in debt with Diego Alonso and Luis S. Lorente for their help with theory and verification of results, and with an anonymous referee for various comments on an earlier version of the manuscript, which helped to improve both the presentation of the results and the overall readability of the paper.

References

[1] D.J. Lucia, P.S. Beran, W.A. Silva, Reduced-order modeling: new approaches for computational physics, Progress in Aerospace Sciences 40 (2004) 51–117.
[2] J.S.R. Attonen, P.I. King, P.S. Beran, POD based reduced-order models with deforming grids, Mathematical and Computer Modelling 38 (1–2) (2003) 41–62.
[3] W.A. Silva, R.E. Bartels, Development of reduced-order models for aeroelastic analysis and flutter prediction using the CFL3D v6.0 code, Journal of Fluids and Structures 19 (2004) 729–745.
[4] J. Vierendeels, L. Langose, J. Degroote, P. Verdonck, Implicit coupling of partitioned fluid–structure interaction problems with reduced order models, Computers and Structures 85 (2007) 970–976.
[5] S. Niroomandi, I. Alfaro, E. Cueto, F. Chinesta, Real-time deformable models of non-linear tissues by model reduction techniques, Computer Methods and Programs in Biomedicine 91 (2008) 223–231.
[6] J.J. Hollkamp, R.W. Gordon, Reduced-order models for non-linear response prediction: implicit condensation and expansion, Journal of Sound and Vibration 318 (2008) 1139–1153.
[7] M.P. Mignolet, C. Soize, Stochastic reduced-order models for uncertain geometrically nonlinear dynamical systems, Computer Methods in Applied Mechanics and Engineering 197 (2008) 3951–3963.
[8] Y. Rouizi, Y. Favennec, J. Ventura, D. Petit, Numerical model reduction of 2D steady incompressible laminar flows: application on the flow over a backward-facing step, Journal of Computational Physics 228 (2009) 2239–2255.
[9] O. Balima, Y. Favenenec, M. Girault, D. Petit, Comparison between modal identification method and the POD Galerkin method for model reduction in nonlinear diffusive systems, International Journal for Numerical Methods in Engineering 67 (2006) 895–915.
[10] Z. Ma, C.W. Rowley, G. Tadmor, Snapshot based balanced truncation for linear time periodic systems, IEEE Transactions on Automatic Control 55 (2010) 469–473.
[11] H. Sandberg, An extension to balanced truncation with application to structured model reduction, IEEE Transactions on Automatic Control 55 (2010) 1038–1043.
[12] D. Alonso, A. Velazquez, J.M. Vega, Robust reduced order modeling of heat transfer in a back-step flow, International Journal of Heat and Mass Transfer 52 (2009) 1149–1157.
[13] D. Alonso, A. Velazquez, J.M. Vega, A method to generate computationally efficient reduced order models, Computer Methods in Applied Mechanics and Engineering 198 (2009) 2683–2691.
[14] H.I. Abu-Malaweh, A review of research on laminar mixed convection flow over a backward and forward facing steps, International Journal of Thermal Sciences 42 (2003) 897–909.
[15] A. Velazquez, J.R. Arias, B. Mendez, Laminar heat transfer enhancement downstream of a backward facing step by using a pulsating flow, International Journal of Heat and Mass Transfer 51 (2008) 2075–2089.
[16] B.F. Armaly, F. Durst, J. Pereira, Experimental and theoretical investigation of backward-facing step flow, Journal of Fluid Mechanics 127 (1983) 473–496.
[17] F. Durst, J.C.F. Pereira, Time-dependent laminar backward-facing step flow in a two dimensional duct, Journal of Fluids Engineering 110 (1988) 289–296.
[18] D. Barkley, M.G.M. Gomes, R.D. Henderson, Three-dimensional instability in flow over a backward-facing step, Journal of Fluid Mechanics 473 (2002) 167–190.
[19] B. Mendez, A. Velazquez, Finite point solver for the simulation of 2-D laminar incompressible unsteady flows, Computer Methods in Applied Mechanics and Engineering 193 (2004) 825–848.
[20] Y. Kim, D. Rockwell, A. Liakopoulos, Vortex buffeting of aircraft tail: interpretation via proper orthogonal decomposition, AAIA Journal 43 (2005) 550–559.
[21] L.S. Lorente, J.M. Vega, A. Velazquez, Generation of aerodynamics databases using Singular Value Decomposition, Journal of Aircraft 45 (2008) 1779–1788.
[22] T. Bui-Thanh, Proper orthogonal decomposition extensions and their applications in steady aerodynamics, Master thesis: Singapore-MIT Alliance (2003).